Applied Catalysis B: Environmental 165 (2015) 378–388

Contents lists available at ScienceDirect

Applied Catalysis B: Environmental

journal homepage: www.elsevier.com/locate/apcatb

A general method to diverse silver/mesoporous–metal–oxide nanocomposites with plasmon-enhanced photocatalytic activity

Tongxuan Liu [a], Benxia Li [a,*], Yonggan Hao [a], Fang Han [b], Linlin Zhang [c], Luyang Hu [a]

[a] School of Materials Science and Engineering, Anhui University of Science and Technology, Huainan, Anhui 232001, PR China
[b] Anhui Entry-Exit Inspection and Quarantine Bureau, 329 Tunxi Road, Hefei, Anhui 230029, PR China
[c] School of Chemistry Engineering, Anhui University of Science and Technology, Huainan, Anhui 232001, PR China

ARTICLE INFO

Article history:
Received 11 August 2014
Received in revised form 9 October 2014
Accepted 14 October 2014
Available online 23 October 2014

Keywords:
Mesoporous structure
Metal oxide
Silver nanoparticles
Surface plasmon resonance
Photocatalytic activity

ABSTRACT

Incorporating plasmonic Ag nanoparticles into mesoporous metal–oxide (MMO) semiconductors will achieve collective effect to greatly increase the photocatalysis. This work demonstrated a general two-step method to obtain diverse Ag/MMO composite photocatalysts with plasmon-enhanced photocatalytic activity. Several typical MMO (TiO_2, ZnO, and CeO_2) semiconductors were synthesized by integrating evaporation-induced self-assembly and *in situ* pyrolysis of metal precursors. Different amounts of Ag nanoparticles were then loaded in these MMO semiconductors through a facile photodeposition process. The Ag nanocrystals with sizes of 50–100 nm were embedded in MMO semiconductors, endowing the Ag/MMO composites notable visible light absorption. The photocatalytic activities of the as-prepared diverse photocatalysts were studied systematically. The influencing factors including MMO species, mesoporous structure, and Ag loading amount on the photocatalytic activity were discussed in detail. The Ag/MMO composites exhibited much improved photocatalytic activity than their pure MMO semiconductors. The mesoporous TiO_2 with the Ag-loading amount of 5 wt.% exhibited the best photocatalytic performance for photodegrading both methylene blue and phenol under a simulated sunlight. The enhancement in photocatalysis is attributed to the synergistic effect of the mesoporous structures for efficient mass transfer as well as the Ag nanoparticles providing plasmonic enhanced light absorption.

1. Introduction

Mesoporous materials have attracted considerable attention for their broad applications in catalysis [1,2], energy conversion and storage [3–6], sensors [7–9], and so on, due to their large surface areas, tunable pore sizes and shapes, various structures, multitude of compositions, and ease of functionalization [6,10]. Mesoporous metal oxide (MMO) semiconductors are gaining popularity for photocatalytic applications due to their large specific surface area in a continuous structure instead of discrete particles [11–13]. The mesoporous feature is expected to greatly facilitate the light harvesting, photogenerated charge carriers transfer, and carrier-induced surface reaction, resulting in higher photocatalytic activity [14,15]. However, the single-component semiconductor photocatalysts are encountering bottlenecks in improving their solar-driven catalytic efficiency due to their inherent limitations such as the high rate of charge-carrier recombination and limited light absorption. In this regard, developing the hybrid nanocomposites with synergistic effects is an effective approach to make a breakthrough in the photocatalytic performance of semiconductor photocatalysts.

Silver nanoparticles, an accessible noble metal nanomaterial, have recently proven to be promising in harvesting photon energy for chemical reactions due to their extraordinary localized surface plasmon resonance (LSPR) properties in the visible light region [16–18]. The energetic electron-driven photocatalysis of silver nanostructures have been demonstrated in the catalytic oxidation reactions [19] and water-splitting [20] under visible light irradiation. The researches in recent years have demonstrated that the incorporation of plasmonic Ag nanocrystals in semiconductor nanostructures can gain greatly improved photocatalytic performance due to the LSPR-induced light focusing in the vicinity of Ag nanocrystals and/or plasmon-sensitized photocatalysis of semiconductors [21–23]. Moreover, the photogenerated charge carriers can be efficiently separated at the interface between Ag and semiconductor, which allows the efficient formation of

* Corresponding author. Tel.: +86 554 6668649; fax: +86 554 6668643.
E-mail address: libx@mail.ustc.edu.cn (B. Li).

http://dx.doi.org/10.1016/j.apcatb.2014.10.041
0926-3373/

reactive oxygen species for the degradation of organic compounds [24,25]. Therefore, coupling metal oxide semiconductors with silver nanoporticles presents a promising strategy for designing advanced photocatalysts and elicits widespread research interest [26,27]. Awazu et al. deposited TiO_2 film on nanoparticles comprising an Ag core covered with a silica (SiO_2) shell to prevent oxidation of Ag by direct contact with TiO_2 [28]. The most appropriate diameter for Ag nanoparticles and thickness for the SiO_2 shell giving rise to LSPR in the near UV were estimated from Mie scattering theory. The photodegradation rate of methylene blue (MB) on such a film was increased by a factor of 7 under near-UV illumination. Kumar et al. investigated the effect of the silica layer thickness on the overall photocatalytic performance of TiO_2 (15 nm)/SiO_2/Ag nanoparticle architectures by use of atomic layer deposition to achieve precise film thickness of SiO_2 and TiO_2 layers [29]. The composite photocatalyst with a 2 nm SiO_2 interlayer exhibited the best photocatalytic performance, suggesting that the plasmonic near-field enhancement effect plays a dominant role. Besides, the plasmonic photocatalysts composed of Ag/AgX (X = Cl, Br, I) loaded on metal–oxide supports were prepared by the simple ion-exchange and the light-induced chemical reduction methods, in which the supports with hierarchical nanostructures could endow higher surface-to-volume ratio and more reactive sites to the photocatalysts [30,31].

In particular, the MMO nanomaterials are fascinating to act as functional supports for fabricating plasmonic composite photocatalysts. It has been demonstrated that the Ag nanoparticles synthesized within the mesopore structure of SBA-15 by microwave-assisted alcohol reduction displayed controllable sizes and color, having enhanced catalytic activity under visible light irradiation owing to LSPR, compared to Ag NPs obtained by pure thermal processes [32]. The integration of plasmonic Ag nanoparticles and MMO semiconductors would obtain a further efficient utilization of Ag nanoparticles and enhance photocatalytic activity in a most effective way [33–35]. The synthesis of various Ag/MMO composite photocatalysts *via* a general route is of great significance for facilitating the studies of the plasmon-enhanced photocatalysis and thereby guiding the design and creation of advanced photocatalysts, but a challenge as well. Based on these considerations, the present work demonstrates a facile and general two-step method to obtain diverse Ag/MMO composite photocatalysts with plasmon-enhanced photocatalytic activity. The photocatalytic activities of the Ag/MMO nanocomposites were evaluated by photodegrading methylene blue (MB) and phenol in aqueous solution under a simulated sunlight. The Ag/MMO composites exhibited much enhanced photocatalytic activity than their corresponding pure MMO semiconductors. Moreover, the mesoporous TiO_2 with the Ag-loading amount of 5 wt.% exhibited the best photocatalytic activity. This work not only provides a general method for preparing Ag/MMO composite photocatalysts but also sheds some light on the plasmon enhancement in photocatalysis by the synergistic effect between plasmonic metal nanoparticles and MMO semiconductors.

2. Experimental

2.1. Materials

All the chemicals are analytical reagent and used as received without further purification. Triblock copolymer Pluronic F127 ($EO_{106}PO_{70}EO_{106}$; EO: ethylene oxide; PO: propylene oxide) was purchased from Sigma–Aldrich. Coumarin ($C_9H_6O_2$) was purchased from Aladdin Reagents (Shanghai) Co., Ltd. Zinc nitrate hexahydrate [$Zn(NO_3)_2{\cdot}6H_2O$], cerous nitrate [$Ce(NO_3)_3{\cdot}6H_2O$], tetrabutyl orthotitanate [$Ti(OBu)_4$], silver nitrate ($AgNO_3$), concentrated hydrochloric acid (HCl, 37 wt.%), and absolute alcohol were purchased from Shanghai Sinopharm Chemical Reagent Co., Ltd. Deionized water was used throughout this work.

2.2. Synthesis of MMO semiconductors (MO = ZnO, TiO_2 and CeO_2)

All the MMO samples were synthesized using a general process integrating evaporation-assisted self-assembly and *in situ* pyrolysis of metal precursors. In a typical synthesis, 0.5 g of Pluronic F127 were dissolved in 15 mL of absolute alcohol (EtOH), and then 5 mmol of the respective metal precursor (Table 1) was added into the solution with vigorous stirring. For the synthesis of mesoporous TiO_2, 3 mL of concentrated hydrochloric acid was used to restrain the hydrolyzation of $Ti(OBu)_4$. The resulting solution was kept in an oven at 50 °C for 24 h, and then dried at 100 °C for 6 h. The as-made xerogels were then calcined at 400 °C for 4 h to remove the block copolymer surfactant species, with a heating rate of 1 °C/min from room temperature. Finally, the MMO samples were obtained.

2.3. Preparation of Ag/MMO (MO = ZnO, TiO_2 and CeO_2) nanocomposites

The Ag/MMO (MO = ZnO, TiO_2 and CeO_2) nanocomposites were prepared through a facile and eco-friendly photodeposition process. Before photodeposition, a certain amount (~0.24 g) of MMO powder was dispersed in deionized water (15 mL) to form a suspension. An $AgNO_3$ aqueous solution with concentration of 3.936 mg/mL (the equivalent concentration of Ag is 2.5 mg/mL) was prepared, which was used for all of the Ag loading experiments. For the preparation of Ag/MMO nanocomposites, the $AgNO_3$ solution with different amounts was injected into the MMO suspensions under magnetic stirring. The dosage of $AgNO_3$ solution was calculated according to that the theoretical Ag loading mass percent in the targeted composites is 1 wt.%, 2 wt.% and 5 wt.%, respectively. Then, the reaction mixture was irradiated by UV–vis light from a Xe lamp for 30 min under continuous stirring. Finally, the dispersion was centrifuged and washed by deionized water for several times, and then dried at 60 °C.

The as-prepared Ag/MMO samples with different Ag loading amounts were denominated as Ag(*x*)/MMO, where *x* represents the theoretical Ag loading mass percent calculated from the experimental dosage of $AgNO_3$, as shown in Table 2.

2.4. Characterizations

The X-ray diffraction (XRD) patterns were recorded on a Japan Shimadzu XRD-6000 equipped with graphite monochromatized high-intensity Cu Kα radiation (λ = 0.1542 nm), and operated at 40 kV voltage and 30 mA current. The field emission scanning electron microscopy (FESEM) images were performed on JEOL JSM-6700F (Japan) at an accelerating voltage of 20 kV. Transmission electron microscopy (TEM) and high resolution transmission electron microscopy (HRTEM) images associated with the energy-dispersive X-ray (EDX) spectra were obtained on TEM JEOL-2010. X-ray photoelectron spectroscopy (XPS) measurements were performed on a VGESCALAB MKII X-ray photoelectron spectrometer with an exciting source of Mg-Ka. Brunauer–Emmett–Teller (BET) nitrogen adsorption/desorption was measured using a Micromeritics ASAP 2020 V4.01 (V4.01 E) analyzer (USA). The UV–vis diffuse reflection spectra (DRS) of the samples were recorded on a spectrophotometer of Perkin Elmer Lambda 950. The pH values of the solutions for photodeposition of Ag before and after light irradiation were determined on a Colloidal Dynamics Zeta Probe (USA). The actual mass percent of loaded Ag in each Ag/MMO nanocomposites was measured by Inductively Coupled Plasma Optical Emission Spectra (ICP-OES) on a Perkin Elmer Optima 8300 optical emission

Table 1
Preparation conditions and porous properties of mesoporous metal oxides.

Product	Precursor	Surface area[a] (m^2/g)	Pore size[b] (nm)	Pore volume (cm^3/g)[c]
ZnO	$Zn(NO_3)_2{\cdot}6H_2O$	19.78	33.6	0.1849
TiO_2	$Ti(OBu)_4$	145.59	9.16	0.4146
CeO_2	$Ce(NO_3)_3{\cdot}6H_2O$	46.36	6.86	0.0834

[a] BET surface areas determined from the nitrogen adsorption isotherm measurements.
[b] BJH pore diameters determined from the nitrogen adsorption branches.
[c] BJH adsorption cumulative volume of pores between 1.7 nm and 300 nm width.

Table 2
Experimental dosages and ICP-OES measured Ag loading of Ag(*x*)/MMO samples prepared by the photodeposition method.

Sample	Experimental dosage of MMO (g)/Ag[a] (mg)	Theoretical Ag loading[b] (wt.%)	Measured Ag loading amounts[c] (mg)	Measured Ag loading[d] (wt.%)
Ag(*1*)/ZnO	0.2475/2.5	1.0	1.9	0.76
Ag(*2*)/ZnO	0.2450/5.0	2.0	4.7	1.88
Ag(*5*)/ZnO	0.2375/12.5	5.0	10.9	4.36
Ag(*1*)/TiO_2	0.2475/2.5	1.0	2.0	0.80
Ag(*2*)/TiO_2	0.2450/5.0	2.0	4.5	1.80
Ag(*5*)/TiO_2	0.2375/12.5	5.0	10.9	4.36
Ag(*1*)/CeO_2	0.2475/2.5	1.0	1.9	0.76
Ag(*2*)/CeO_2	0.2450/5.0	2.0	4.6	1.84
Ag(*5*)/CeO_2	0.2375/12.5	5.0	11.0	4.40

[a] The data are calculated from the usage of $AgNO_3$ for each sample synthesis.
[b] The mass percentage of Ag calculated from the experimental usages of $AgNO_3$ and MMO for each sample.
[c] The data are calculated from the ICP-OES results.
[d] The mass percentage of Ag in each sample from the ICP-OES measured results.

spectrometer (USA), in which the analyte is the Ag emission spectrum at 328.068 nm.

2.5. Tests for the photocatalytic activity of Ag/MMO nanocomposites

The photocatalytic properties of the as-prepared materials were evaluated by photodegrading the representative organic pollutants of MB and phenol in water under a simulated sunlight. A Xe lamp (CEL-HXF300, Beijing China Education Au-light Co., Ltd) equipped with a long-pass reflector was utilized to provide the broadband light irradiation (λ = 350–780 nm) which is well coincident with the dominating light wavelength region of natural sunlight. In each test, 50 mg of photocatalyst was suspended in 100 mL of MB aqueous solution (20 mg/L) or phenol aqueous solution (20 mg/L). The suspension was exposed to the light irradiation under magnetic stirring, after stirred in dark for 2 h to achieve adsorption-desorption equilibrium between photocatalyst and organic pollutant. At given time intervals, about 3 mL of solution was sampled for analyzing the pollutant concentration. The photocatalytic degradation process was monitored using a UV–vis spectrophotometer (Shimadzu UV-2600) to record the characteristic absorption of MB (665 nm) and phenol (269 nm).

2.6. Assays for the produced hydroxyl radicals during photocatalytic process

The photogeneration of hydroxyl radicals (•OH) in the presence of several typical photocatalysts of MMO and Ag(*5*)/MMO was measured by a fluorescence probe method with coumarin ($C_9H_6O_2$) which can turn into fluorescent umbelliferone upon reaction with •OH radicals. The optimum excitation wavelength (λ_{ex}) and the maximum emission peak wavelength (λ_{em}) of umbelliferone are determined to be 372 nm and 478 nm, respectively. For a typical process, 100 mg of a photocatalyst (MMO or Ag(*5*)/MMO) was dispersed in 100 mL of coumarin solution (1×10^{-3} M) with constant stirring. The suspension was irradiated by the same light source used in the photocatalytic degradation process. At a given time interval (30 min), about 2 mL of the solution was sampled and monitored its maximum photoluminescence emission intensity at 478 nm under the optimum excitation at 372 nm on a fluorescence spectrophotometer (F-380, Tianjin Gangdong Sci. & Tech. Development. Co., Ltd, China).

3. Results and discussions

The MMO samples including ZnO, TiO_2 and CeO_2 were synthesized *via* the general route integrating evaporation-induced self-assembly and *in situ* pyrolysis of metal precursors [36,37]. A typical formation process of the MMO samples is illustrated in Scheme 1. The respective metal precursor, triblock copolymer F127 and absolute ethanol were mixed together to form a transparent solution at room temperature. This solution was kept in an oven at 50 °C for 24 h, to achieve the adequate coordination between metal ions and oxygen containing groups of F127 molecules. After that, the solution was then maintained at 100 °C for 6 h in air. During this process, anhydrous ethanol was evaporated and the xerogel of the metal-F127 hybrids formed. Finally, the organic substances in the xerogel were removed by combusting and the metal precursors were pyrolyzed *in situ* to form mesoporous metal oxides.

3.1. Phases and microstructures of pure MMO semiconductors

The phase compositions and crystal structures of the mesoporous metal oxides were characterized by powder X-ray diffraction (XRD). The XRD patterns in Fig. 1 identify these products as the wurtzite phase of ZnO (JCPDS No. 75-1526), anatase phase of TiO_2 (JCPDS No. 89-4921), and cubic phase of CeO_2 (JCPDS No. 81-0792), respectively. The XRD patterns indicate that these samples have high crystallinity and pure crystal phase. SEM and TEM images in Fig. 2 clearly demonstrate the mesoporous structures of the as-obtained MMO samples. These samples appear to be 3D porous cotton-like bulk materials with rough surface, as shown in Fig. 2a–c. ZnO and TiO_2 present similar morphology, while CeO_2 has many large pores with sizes in 100–500 nm on its surface. TEM images (Fig. 2d–f) further reveal that the interior of these cotton-like bulk materials presents mesoporous structures forming by the random attachment of the nanoparticles which have sizes of 10–50 nm for ZnO (Fig. 2d), 5–10 nm for TiO_2 (Fig. 2e) and CeO_2 (Fig. 2f), respectively.

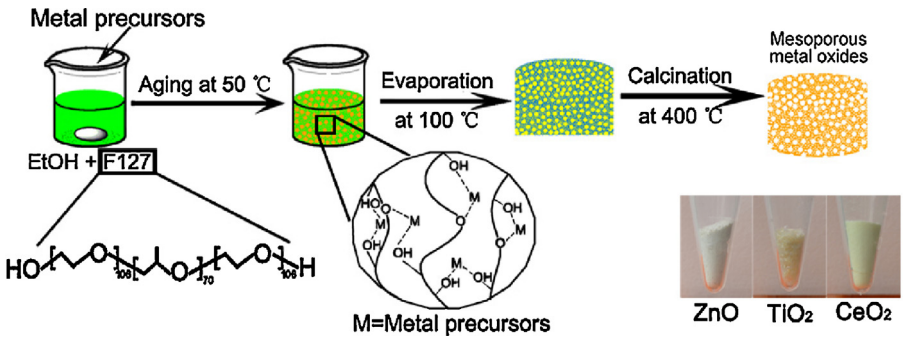

Scheme 1. Schematic procedure for the formation of the mesoporous metal oxides.

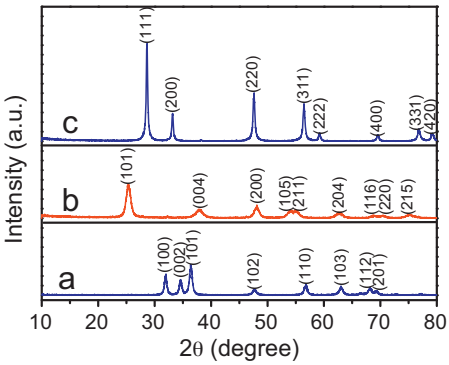

Fig. 1. XRD patterns of (a) mesoporous ZnO, (b) mesoporous TiO_2, and (c) mesoporous CeO_2.

To further examine the mesoporous structure of the MMO products, nitrogen adsorption–desorption isotherms and the corresponding Barrett–Joyner–Halenda (BJH) pore size distribution were measured. The results are shown in Fig. 3 and summarized in Table 1. Nitrogen adsorption measurements demonstrate that all the MMO materials exhibit the type IV isotherm behavior with high Brunauer–Emmett–Teller (BET) surface areas of 19.78 m^2/g for ZnO, 145.59 m^2/g for TiO_2, and 46.36 m^2/g for CeO_2, respectively. The Barrett–Joyner–Halenda (BJH) pore sizes determined from the adsorption branches are 33.6 nm for ZnO, 9.16 nm for TiO_2, and 6.86 nm for CeO_2, respectively. The relative lower surface area and larger pore size of ZnO sample are mainly because that this sample is composed of nanoparticles with larger sizes than those in TiO_2 and CeO_2, as observed from TEM images (Fig. 2d–f).

3.2. Formation and characterizations of Ag/MMO nanocomposites

Subsequently, we succeeded in preparation of the diverse Ag/MMO composite photocatalysts by a facile photodeposition process [25,38], in which the metal loading on semiconductor can be controlled by adjusting the addition of metal sources. The typical formation procedure of the Ag/MMO nanocomposites is illustrated in Scheme 2. The MMO semiconductor is photoexcited under UV–vis illumination to produce electrons for reduction of ionic silver (Ag^+) in aqueous solution to metallic silver (Ag^0) on MMO surface, according to the reactions listed in Eqs. (1)–(3)

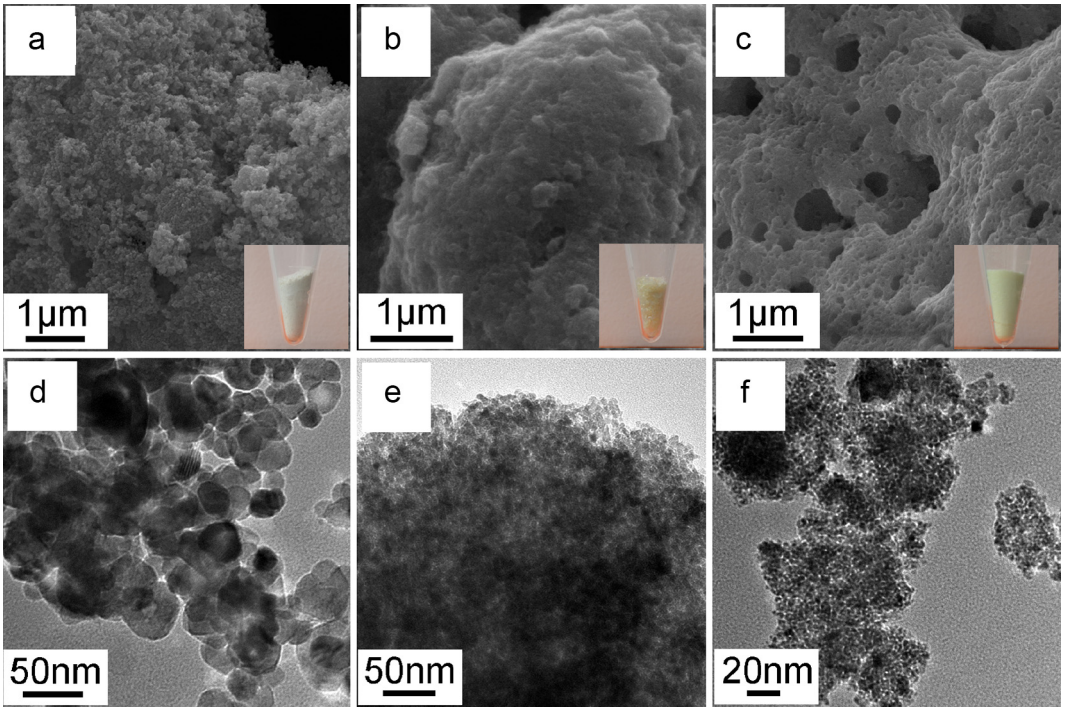

Fig. 2. SEM images (a–c) and TEM images (d–f) of the as-obtained MMO samples: (a and d) mesoporous ZnO, (b and e) mesoporous TiO_2, and (c and f) mesoporous CeO_2. The inserts are the photographs of the respective MMO sample.

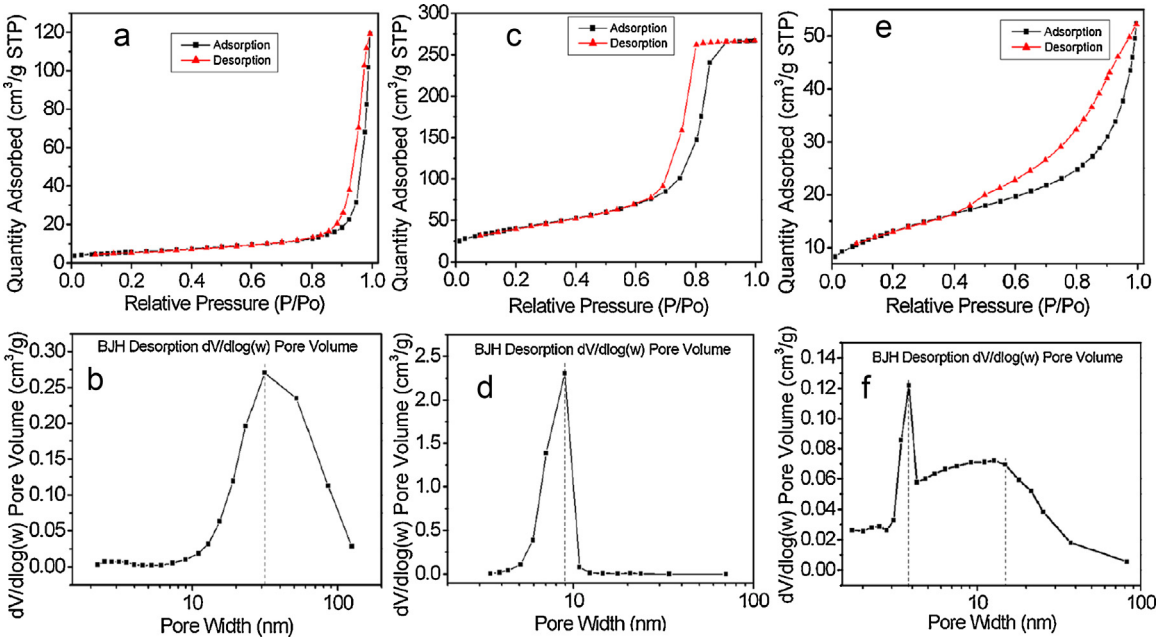

Fig. 3. N_2 adsorption–desorption isotherms at 77 K (a, c, and e) and pore diameter distribution (b, d, and f) of pure MMO: (a and b) mesoporous ZnO, (c and d) mesoporous TiO_2, and (e and f) mesoporous CeO_2.

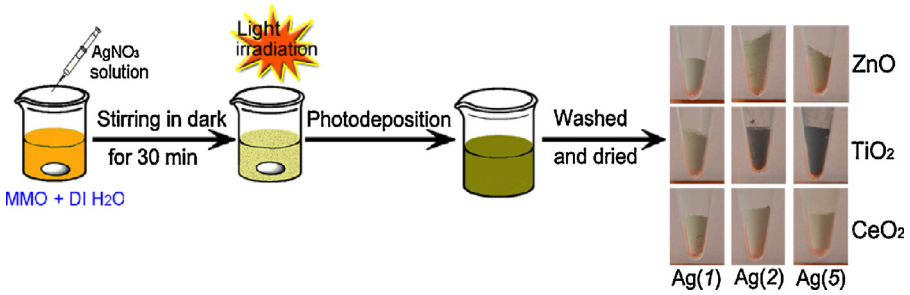

Scheme 2. Schematic procedure for the formation of the Ag(x)/MMO nanocomposites.

below (using Ag/ZnO as an example) [25,39]. To further confirm the photodeposition mechanism in the aqueous solution, the pH values of the solution before and after photodeposition were measured by using Zeta Probe, respectively. The pH value of the reaction solution decreased from 6.2 to 2.1 after UV–vis illumination for 30 min, indicating the formation of HNO_3 during the photoreaction (Eqs. (4)–(6)). After the photodeposition, the colors of the as-obtained samples are obviously different from those of the pure MMO samples, due to the presence of metallic silver nanoparticles. The color of the as-obtained Ag(x)/MMO sample becomes deeper as increasing the dosages of $AgNO_3$ used for the photodeposition, as shown by the photographs in Scheme 2, suggesting the increased Ag loading amounts in MMO.

$$ZnO \xrightarrow{h\nu} ZnO(h_{(photo)}{}^{+} + e_{(photo)}{}^{-}) \quad (1)$$

$$AgNO_3 \xrightarrow{aq} Ag_{(aq)}{}^{+} + NO_{3\,(aq)}{}^{-} \quad (2)$$

$$Ag_{(aq)}{}^{+} + e_{(photo)}{}^{-} \rightarrow Ag^0 \quad (3)$$

$$H_2O + h_{(photo)}{}^{+} \rightarrow H^{+} + {}^{\bullet}OH \quad (4)$$

$$2HO^{\bullet} \rightarrow H_2O + \tfrac{1}{2}O_2 \quad (5)$$

$$H^{+} + NO_{3\,(aq)}{}^{+} \rightarrow HNO_{3\,(aq)} \quad (6)$$

In the XRD patterns of the as-obtained Ag(x)/MMO samples (Fig. 4 and Fig. S1 in the Supporting Information), besides the diffraction peaks of each metal oxide, some new diffraction peaks

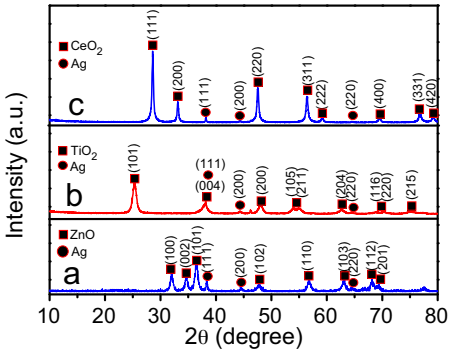

Fig. 4. XRD patterns of the as-prepared Ag(x)/MMO nanocomposites: (a) Ag(5)/ZnO, (b) Ag(5)/TiO_2, and (c) Ag(5)/CeO_2.

assigned to the face centered cubic (fcc) silver (JCPDS No. 87-0720) are observed. XRD results indicate that the metallic silver is incorporated into these MMO samples instead of forming Ag in lattices of MMO because the diffraction peaks of the metal oxides maintain unchanged after Ag loading. Moreover, the diffraction peaks of metallic silver in Ag(x)/MMO samples get stronger with the increased dosage of $AgNO_3$ used for the photodeposition (Fig. S1 in the Supporting Information), which is coincident with the gradually changing color of the Ag(x)/MMO samples shown in Scheme 2. These phenomena probably result from the increased

amount of metallic silver in MMO. ICP-OES measured results shown in Table 2 reveal the Ag loading amount in each Ag(*x*)/MMO sample. The measured content of Ag in each Ag(*x*)/MMO nanocomposite presents a little smaller than its theoretical Ag content calculated from the dosages of $AgNO_3$ for the photodeposition, because Ag^+ ions in the aqueous solution was not entirely photoreduced in the given irradiation time [40].

The typical SEM images of Ag(*5*)/MMO nanocomposites are shown in Fig. 5a–c and those of other Ag(*x*)/MMO samples are shown in Fig. S2 (Supporting Information). These Ag(*x*)/MMO composites present similar morphology with their corresponding MMO materials, maintaining the 3D porous cotton-like appearance with rough surface. Some darker gray nanoparticles observed from the TEM images (Fig. 5d–f) could be determined as Ag nanoparticles embedded among the tiny nanoparticles of MMO. The particle sizes of Ag nanoparticles are in the range of 50–100 nm, much larger than those of the metal oxides. The larger particle sizes of Ag nanoparticles in the nanocomposites will result in stronger LSPR effect [41]. More detailed information was typically obtained from the high resolution TEM (HRTEM) and energy-dispersive X-ray spectra (EDX) of Ag(*5*)/ZnO sample, as shown in Fig. 6. The HRTEM image (Fig. 6b) recorded on the smaller nanoparticles with lighter gray color (the circle-marked area in Fig. 6a) exhibits well-resolved lattice fringe with the spacing of 0.246 nm, corresponding to the interplanar spacing of (1 0 1) lattice plane of hexagonal ZnO. The EDX spectrum (Fig. 6c) recorded on this area further confirms that these smaller nanoparticles are ZnO. For the larger nanoparticles marked by a square framework in Fig. 6a, well defined HRTEM image is failed to obtain because of its large thickness, while the EDX spectrum (Fig. 6d) taken on this nanoparticle shows that the peaks of Ag element are very high and sharp, revealing it is Ag nanoparticle. In Fig. 6d, the weaker signals corresponding to Zn and O result from ZnO nanoparticles covered on the Ag nanoparticle.

The elemental composition and chemical state of Ag(*5*)/mesoporous-ZnO sample were typically investigated by XPS measurement. The XPS survey spectrum (Fig. 7a) shows the presence of only Zn, O, Ag and C elements. No other impurity element exists. The high resolution spectrum (Fig. 7b) of Zn 2p with specific peaks at 1021.20 eV for $2p_{3/2}$ indicates the oxidation state of Zn^{2+} in the form of ZnO in this sample [25,42]. In Fig. 7c, the peak at 530.18 eV is assigned to the lattice oxygen in ZnO, whereas the peak at 531.60 eV can be assigned to surface hydroxyl groups of ZnO [25]. Fig. 7d shows the high resolution Ag 3d spectrum of the Ag nanoparticles in the Ag(*5*)/mesoporous-ZnO nanocomposite, presenting two individual peaks at 367.65 eV for Ag $3d_{5/2}$ and at 373.62 eV for Ag $3d_{3/2}$, which confirms the formation of metallic Ag^0 by the photo-reduction of Ag^+ ions in aqueous solution [43]. The positions of Ag 3d peaks for the Ag/ZnO composite shift obviously to lower binding energies compared with those of the pure metallic Ag (Ag $3d_{5/2}$, 368.2 eV; Ag $3d_{3/2}$, 374.2 eV), which is similar to the results obtained from the Ag/ZnO heterostructures reported previously [44,45]. The binding energy shifts of Ag in the Ag/ZnO composite mainly arise from the electron transfer from Ag nanoparticles to the conduction band of ZnO at their interfaces, because the work function of metallic Ag (4.26 eV) is smaller than that of ZnO (5.3 eV) [46,47]. The equilibration between the Fermi levels of Ag and ZnO in Ag/ZnO composite causes a decrease in the electron density of Ag nanoparticle, and thus the binding energies of Ag 3d in the composite are lower than those of pure metallic Ag. The results further verify the formation of Ag/metal–oxide composite. Therefore, all the above characterized results indicate that the as-obtained Ag/MMO nanocomposites are composed of larger Ag nanoparticles embedded in the mesoporous metal oxides, which is advantageous for the integration of the mesoporous structures for efficient mass transfer and the Ag nanoparticles providing plasmonic enhancement of light absorption and plasmonic sensitization of photocatalysis.

In order to demonstrate the effect of the presence of Ag nanoparticles on the photo-response of the as-obtained Ag/MMO nanocomposites, the UV–vis diffuse-reflectance spectra (DRS) of the pure MMO and Ag(*x*)/MMO samples are recorded and shown in Fig. 8, where i, ii, iii, and iv correspond to the respective pure MMO, Ag(*1*)/MMO, Ag(*2*)/MMO, and Ag(*5*)/MMO, respectively. All the pure MMO materials exhibit a strong absorption in UV region, while the Ag(*x*)/MMO composites possess two prominent absorption bands in the UV–vis region. For Ag(*x*)/MMO composites, the UV absorption band can be assigned to the MMO matrix, indicating the wide bandgaps of these MMO semiconductors, and the absorption bands in visible light region can be attributed to the LSPR absorption of Ag nanoparticles [38,48]. The LSPR absorption of Ag nanoparticles becomes more prominent as the Ag loading amount increases in Ag(*x*)/MMO composites. The different location of the LSPR absorption peaks of Ag nanoparticles is due to the different sizes of Ag nanoparticles in Ag(*x*)/MMO composites [17,21]. Moreover, the LSPR absorption peaks broaden evidently because the Ag nanoparticles present a wide range of particle size distribution. The enhanced absorption in visible region will be beneficial to making full use of sunlight for photocatalysis.

3.3. Photocatalytic properties of Ag/MMO nanocomposites

To examine the photocatalytic activity of the as-prepared Ag(*x*)/MMO composites, the photodegradations of two typical organic pollutants including methylene blue (MB) and phenol in water was chosen as model reactions. The initial concentrations of both MB and phenol were 20 mg/L. The photocatalytic reactions were carried out under a simulated sunlight (λ = 350–780 nm) from a Xe lamp which is well coincident with the dominating light wavelength region from natural sunlight. The photocatalytic activity of commercial ZnO and TiO_2 was also tested for comparison. Figs. S3–S5 (Supporting Information) show the time-dependent UV–vis absorption spectra of MB solution under different conditions, where the time "−120 min" means the dark treatment to reach the adsorption–desorption equilibrium between the photocatalyst and MB molecules. The evolutions of UV–vis absorption spectra of MB solution (Figs. S3–S5) in the presence of different photocatalysts (50 mg) and with irradiation for various durations demonstrate that the characteristic absorption of MB at 665 nm decreases rapidly with the irradiation time. Fig. 9a shows the time-dependent degradation plots, and Fig. 9b shows the photodegradation efficiencies after 60 min irradiation. By comparison, some information is concluded as follows. Firstly, the pure MMO materials exhibit much higher photocatalytic activity than that of the corresponding commercial metal oxide. Secondly, ZnO-based and TiO_2-based photocatalysts present higher photocatalytic activity than that of CeO_2-based photocatalysts. Thirdly, for the same MMO matrix, the photodegradation efficiency increases with the Ag loading amount when the latter is no more than 5 wt.%.

Phenol and its derivates which are generally used as raw materials in petrochemical and chemical industries have become one of the most common organic pollutants in water. Herein, the three pure MMO materials and their respective Ag(*5*)/MMO composites were selected as photocatalysts for photodegrading phenol in water. The evolutions in the absorption spectra of phenol solutions along the irradiation time over different catalysts are shown in Fig. S6 (Supporting Information). The characteristic absorption peak of phenol at 269 nm is used as a reference for analysis. The time-dependent degradation plots and the degradation efficiencies after 120 min irradiation of the simulated sunlight are shown in Fig. 10. The ZnO-based and TiO_2-based photocatalysts exhibit outstanding photocatalytic performance for degrading

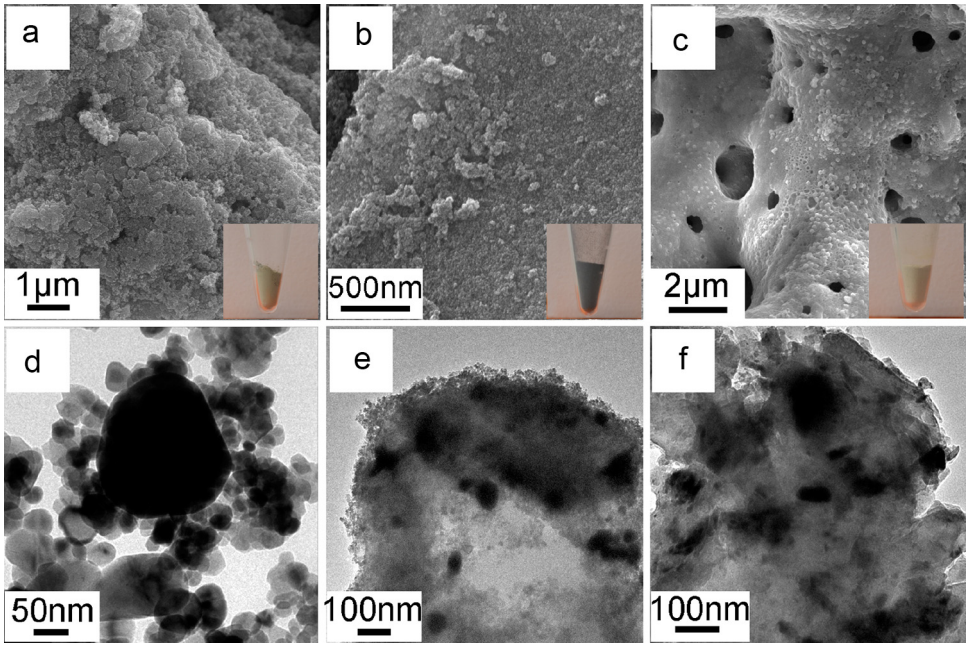

Fig. 5. SEM and TEM images of the as-obtained Ag(5)/MMO samples: (a and d) Ag(5)/ZnO, (b and e) Ag(5)/TiO_2, and (c and f) Ag(5)/CeO_2. The inserts are the corresponding photographs of Ag(5)/MMO samples.

phenol in water. During the photodegradation process, new absorption peaks at 246 nm and 288 nm emerge and then disappear (Fig. S6a–d, Supporting Information), which is attributed to the formation and fading of benzoquinone (maximum absorption peak at 246 nm) and hydroquinone (maximum absorption peak at 288 nm), as shown in Fig. 11 [49,50]. After 120 min irradiation, the degradation efficiencies of phenol over Ag(5)/mesoporous-ZnO and Ag(5)/mesoporous-TiO_2 are 89.79% and 98.96%, respectively, much greater than those over the pure mesoporous ZnO and TiO_2. However, in the case of CeO_2-based photocatalysts, a slight increase in the absorption intensity ($C_t/C_0 > 1.0$) of phenol solution is observed instead (Fig. S6e and f, Supporting Information), which probably arises from the generation of some hydroxylated phenol derivates (such as pyrocatechol and resorcinol) with absorption around 269 nm [49–51]. These hydroxylated phenol derivates cannot be further degraded into smaller organic molecule acids or inorganic molecules (H_2O and CO_2) because the inferior photocatalytic capacity of the CeO_2-based catalysts, as demonstrated in photodegradation of MB (Fig. 9a and b). In addition, the photocatalytic activities of the Ag(x)/mesoporous-TiO_2 composites with higher

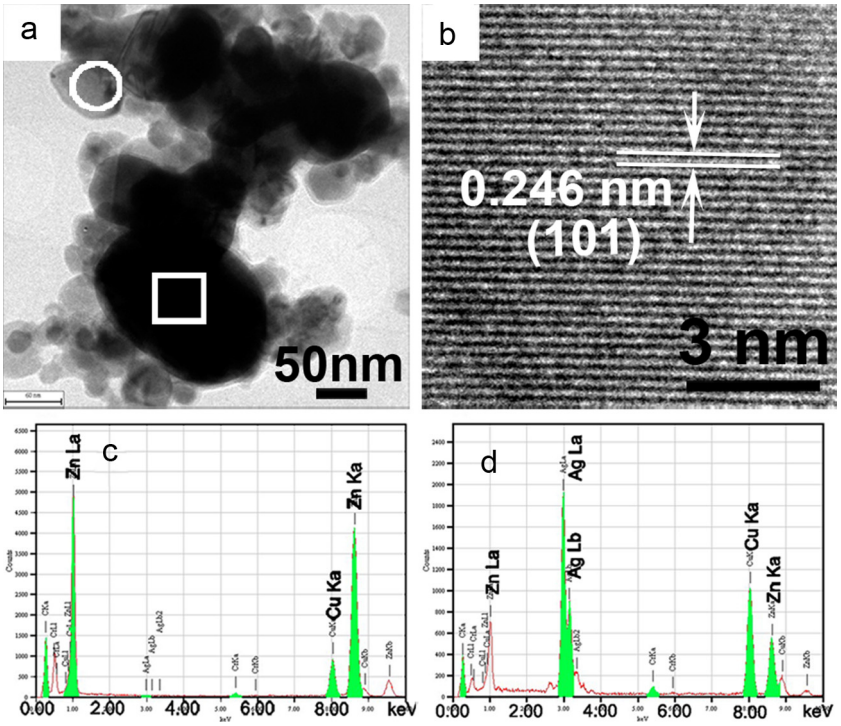

Fig. 6. (a) A TEM image with low magnification of Ag(5)/ZnO sample, (b) HRTEM image and (c) EDX spectrum of the circle-marked area in (a), (d) EDX spectrum of the square-framework marked area in (a).

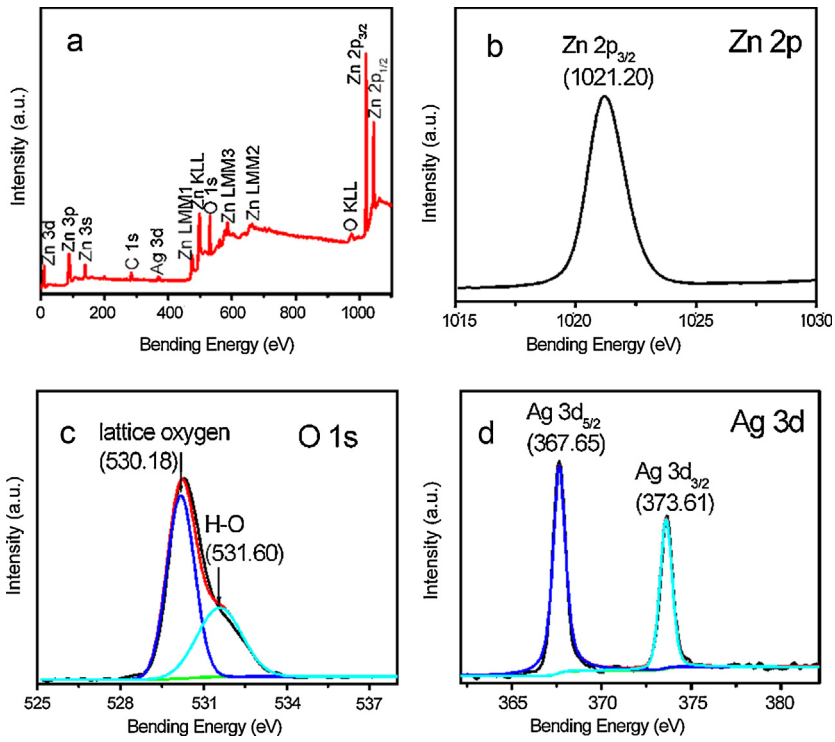

Fig. 7. XPS spectra of Ag(5)/mesoporous-ZnO sample: (a) survey spectrum, (b) Zn $2p_{3/2}$ peak, (c) O 1s peaks, and (d) Ag 3d peaks.

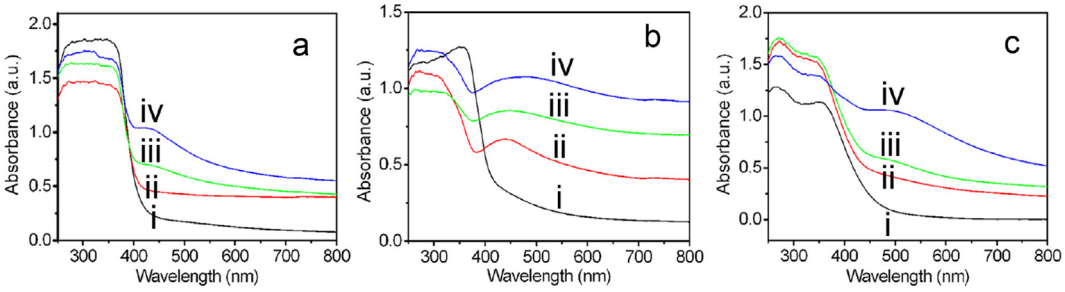

Fig. 8. UV–vis diffuse reflection spectra (DRS) of various pure MMO and Ag(*x*)/MMO samples: (a) Ag(*x*)/mesoporous-ZnO, (b) Ag(*x*)/mesoporous-TiO_2, and (c) Ag(*x*)/mesoporous-CeO_2, where i, ii, iii, and iv represent pure MMO, Ag(*1*)/MMO, Ag(*2*)/MMO, and Ag(*5*)/MMO, respectively.

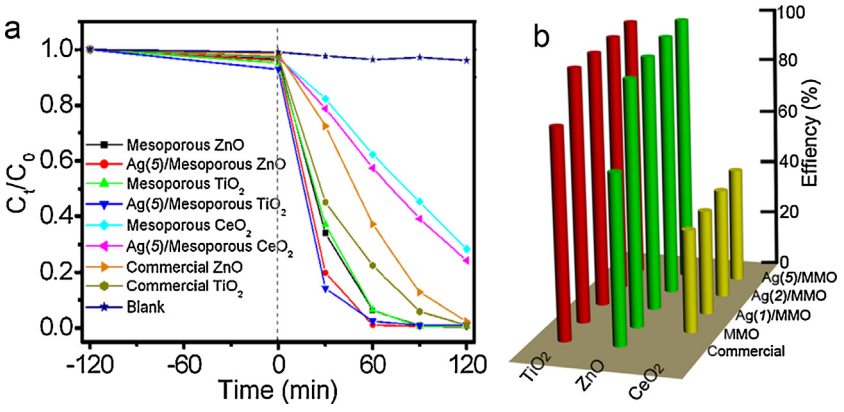

Fig. 9. The results for photocatalytic degrading MB solution (20 mg/L) under the simulated sunlight and other different conditions. (a) Time-dependent degradation plots, (b) the degradation efficiencies after 60 min irradiation.

Ag-loading amounts (10 wt.% and 20 wt.%) were examined by photodegrading phenol in water under the simulated sunlight (Fig. S7 in the Supporting Information), to provide the photocatalytic efficiency trend with the Ag loading increasing. Fig. 10c shows a curve of the photodegradation efficiency after 120 min *versus* Ag loading amount in Ag(*x*)/mesoporous-TiO_2 composite, which depicts that the Ag loading amount has a great influence on the photocatalytic activity of the Ag/MMO composites. The photocatalytic activity

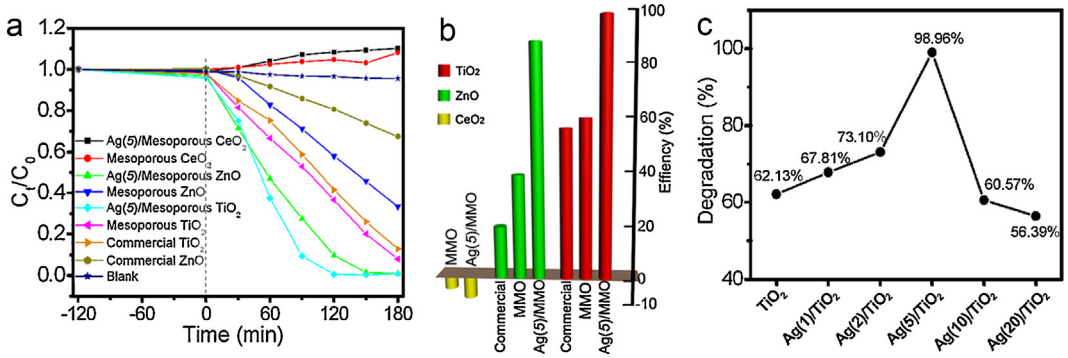

Fig. 10. The results for photocatalytic degrading phonel solution (20 mg/L) under the simulated sunlight and other different conditions. (a) Time-dependent degradation efficiency plots, (b) degradation efficiencies over different photocatalysts after 120 min irradiation, (c) the degradation efficiency after 120 min *versus* Ag loading amount of Ag(x)/TiO_2 composite.

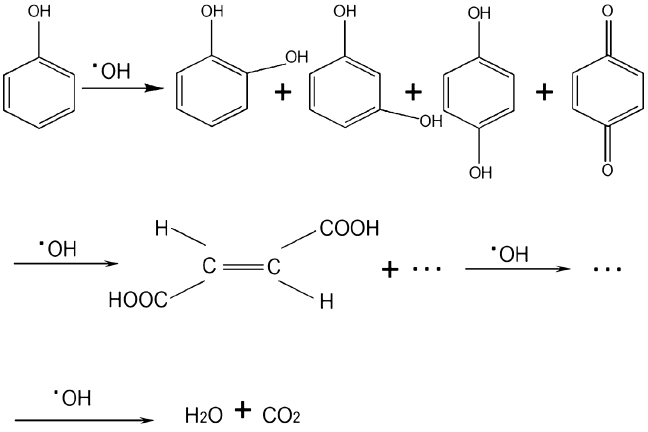

Fig. 11. The pathway of phenol photodegradation.

of the composite initially increases and then decreases with the Ag loading amount increasing. The Ag(5)/mesoporous-TiO_2 composite exhibits the best photocatalytic activity for photodegrading phenol. As a supplement, to further reveal the plasmon-induced enhancement in the visible-light-reponse photocatalytic activity, the photocatalytic reactions of phenol degradation was carried out under a visible light ($\lambda > 420$ nm) from the Xe lamp after removing the wavelength shorter than 420 nm, using the pure mesoporous TiO_2 and Ag(5)/mesoporous-TiO_2 as photocatalysts, respectively. The evolutions in the absorption spectra of phenol solutions along the irradiation time are shown in Fig. S9 (Supporting Information). The pure mesoporous TiO_2 shows a very low photocatalytic capacity under the visible light because of its wide band gap. But the Ag(5)/mesoporous-TiO_2 catalyst shows a greatly enhanced photocatalytic activity under the visible light, and the degradation percent of phenol over this catalyst is 85.04% after 210 min irradiation. The results further confirm that Ag nanoparticles anchored on MMO materials can harvest the photon energy of visible light for the effective degradation of organic pollutants.

In order to further elucidate the different photocatalytic performance of the diverse catalysts and clarify the photocatalytic mechanism, the photogenerated •OH radicals, which are generally considered as the major active species responsible for the photocatalytic oxidation of organic compounds [52], were detected by means of a fluorescence probe method [53]. The reaction of coumarin with •OH radicals can produce the fluorescent umbelliferone, as shown by Fig. S10 (Supporting Information). On the excitation at 372 nm, umbelliferone emits the fluorescence with peak at 478 nm. The fluorescence intensity at 478 nm was measured to determine the concentration of umbelliferone and further evaluate the photogenerated •OH radicals. Fig. S11 (Supporting Information) shows the fluorescence emission spectra of the produced umbelliferone in the solution sampled at various time for several typical photocatalysts including the three pure MMO and the respective Ag(5)/MMO composite. The variation curves for the fluorescence intensity of the produced umbelliferone along the irradiated time are shown in Fig. 12. For each tested photocatalyst, the fluorescence intensity increases steadily with irradiation time, meaning that •OH radicals are continuously generated upon photo-activation. By comparison, Ag(5)/MMO composites exhibit enhanced •OH generation capacities than the corresponding pure MMO materials. Moreover, the mesoporous-ZnO based and mesoporous-TiO_2 based photocatalysts show much superior •OH generation capacities to mesoporous-CeO_2 system, agreement with the results of the above photodegrading experiments. In addition, it is noted that the fluorescence intensity of the produced umbelliferone in the Ag(5)/mesoporous-ZnO and Ag(5)/mesoporous-TiO_2 system decreased after 150 min irradiation, possibly because some of the produced umbelliferone molecule were degraded by excessive •OH radicals.

3.4. Proposed mechanism for the enhanced photocatalytic activity

Based on the above experimental results and evidences, reasonable explanations can be concluded as follows about the mechanism for the enhanced photocatalysis of the Ag/MMO composites, especially Ag/mesoporous-ZnO and Ag/mesoporous-TiO_2. Firstly, the superior photocatalytic performance of mesoporous ZnO and TiO_2 materials than that of the commercial ones can be attributed to their special mesoporous structures for efficient mass transfer. The photocatalytic degradation of the organic pollutants occurs generally in the sequence of diffusion, adsorption, surface reaction, and final desorption, and each of these elementary processes affects the reaction rate. The large surface area and pore volume in the MMO materials offered more opportunity for the diffusion and adsorption of pollutant molecules and hydroxyl radicals during the photocatalytic reaction [1,2]. Moreover, both the large surface area and the good crystallinity in a continuous structure can be expected to make the electron transfer within the material easier, resulting in higher activity [6]. The inferior photocatalytic activity of CeO_2-based catalysts mainly results from the lower carrier mobility of CeO_2 material than those of ZnO and TiO_2 [54,55]. Secondly, the obvious enhancement in the photocatalysis of Ag/MMO composites is mainly due to the plasmonic effect of Ag nanoparticles, as shown in Scheme 3 [56,57]. On one hand, the LSPR in the Ag nanoparticles and the electron–hole pairs in the MMO semiconductors were excited simultaneously by

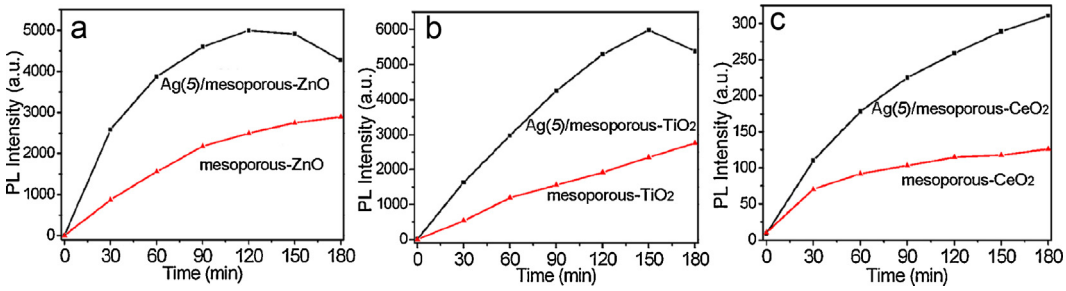

Fig. 12. The variation for the fluorescence intensity of the produced umbelliferone *versus* irradiation time in the presence of different photocatalysts: (a) mesoporous ZnO and Ag(5)/ZnO composite, (b) mesoporous TiO_2 and Ag(5)/TiO_2 composite, (c) mesoporous CeO_2 and Ag(5)/CeO_2 composite.

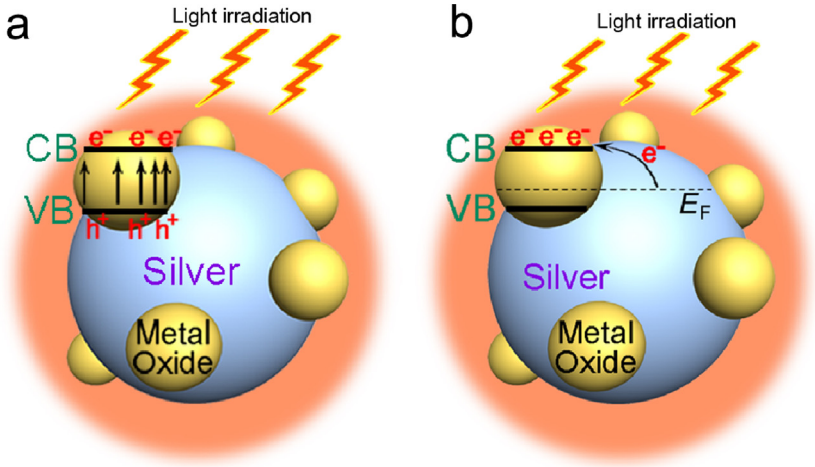

Scheme 3. Schematic presentation of the plasmonic enhancement mechanism for the Ag/MMO photocatalysts: (a) Plasmonic enhancement of light absorption. (b) Plasmonic sensitization (hot-electron effect).

the broadband light (λ = 350–780 nm). The excited Ag nanoparticles generate a strong local electromagnetic field whose intensity is several orders of magnitude higher than that of the far-field incident light. The strong local electromagnetic field strongly enhances the concentration of the electron–hole pairs in the metal oxide in the vicinity of the plasmonic Ag nanoparticles, as shown in Scheme 3a, because the electron–hole pair generation rate is proportional to the local field intensity [56,57]. For this plasmon-induced near-field enhancement effect, Ag nanoparticles in the composites function as antennas which can effectively concentrate the incident photon energy and transfer it to the adjacent semiconductors through the near-field interaction. The electron-hole pairs formation will be strongly enhanced in the adjacent semiconductor, thus enhance the photocatalysis. On the other hand, a plasmon-driven charge separation process, namely plasmonic sensitization, may occur at the interface between plasmonic Ag nanoparticles and the metal oxide semiconductor, as shown in Scheme 3b. The excited plasmon of Ag nanoparticles in the Ag/MMO composites produces hot electrons, some of which have energies higher than the Schottky barrier at the interface and can cross the barrier, injecting into the conduction band of the semiconductor [58]. The plasmonic energy transfer discussed above remarkably enhances the concentration of photogenerated carriers in photocatalyst. The photogenerated electrons and holes were captured by surface-adsorbed O_2 and H_2O, respectively, to generate the reactive oxidation species of •OH radicals in the aqueous solution, and then degrade the organic pollutants efficiently. The plasmonic enhancement effect increases with the Ag loading amount within a certain range, giving rise to higher photocatalytic activity of the Ag/MMO composites. However, redundant Ag nanoparticles in the composites have an unfavorable influence on photocatalysis, probably because the excessive Ag nanoparticles cover the active sites of MMO supports to reduce the availability of pollutant adsorption and act as recombination centers of electron–hole pairs [59]. Based on the discussions above, we believe that the improved photocatalytic performance of Ag/MMO nanocomposites can be attributed to the synergetic effect of the mesoporous structures for efficient mass transfer as well as the Ag nanoparticles providing plasmonic enhancement of light absorption.

4. Conclusions

A series of Ag/MMO composite photocatalysts with plasmon-enhanced photocatalytic activity were prepared by a facile and general process. Several typical MMO semiconductors including TiO_2, ZnO, and CeO_2 are prepared by integrating evaporation-induced self-assembly and *in situ* pyrolysis of metal precursors. Different amounts of Ag nanoparticles (*i.e.* 1 wt.%, 2 wt.%, and 5 wt.%) were then loaded in these MMO semiconductors *via* a eco-friendly photodeposition process. The as-obtained Ag/MMO composites are composed of Ag nanoparticles with sizes of 50–100 nm and surrounded by small nanoparticles of metal oxides. Used for photodegrading the typical organic pollutants of MB and phenol under a simulated sunlight (λ = 350–780 nm), the Ag/MMO composites showed greatly enhanced photocatalytic activity than their corresponding pure MMO semiconductors. Thereinto, the inferior photocatalytic activity of CeO_2-based catalysts, compared with the other Ag/MMO composites, possibly results from the lower carrier mobility of CeO_2 material than those of ZnO and TiO_2. The mesoporous TiO_2 with Ag-loading amount of 5 wt.% exhibits the highest photocatalytic activity. The capacity of photogenerating •OH radicals for each pure MMO material and Ag(*x*)/MMO

composite was evaluated by means of a fluorescence probe method, and the results coincide with those from the photocatalytic degradations of both MB and phonel. The enhancement in the photocatalytic activity of Ag/MMO composites can be attributed to the synergetic effect of the mesoporous structures for efficient mass transfer as well as the Ag nanoparticles providing plasmonic enhancement of light absorption. The present work provides a facile and general method for the fabrication of Ag/MMO and other composite photocatalysts. Moreover, these plasmonic composite photocatalysts with higher activity are expected to be attractive in solar-driven chemical reactions.

Acknowledgments

This work is supported by the National Natural Science Foundation of China (21471004 and 51208003), the Excellent Youth Talents Support Plan in Colleges and Universities of Anhui Province, the Youth Talents Program in Anhui University of Science and Technology, and Postdoctoral Science Foundation of China (2014M551789).

Appendix A. Supplementary data

Supplementary data associated with this article can be found, in the online version, at http://dx.doi.org/10.1016/j.apcatb.2014.10.041.

References

[1] C.M.A. Parlett, K. Wilsonand, A.F. Lee, Chem. Soc. Rev. 42 (2013) 3876–3893.
[2] Y. Shi, C. Hua, B. Li, X. Fang, C. Yao, Y. Zhang, Y.-S. Hu, Z. Wang, L. Chen, D. Zhao, G.D. Stucky, Adv. Funct. Mater. 23 (2013) 1832–1838.
[3] T. Brezesinski, J. Wang, R. Senter, K. Brezesinski, B. Dunn, S.H. Tolbert, ACS Nano 4 (2010) 967–977.
[4] T. Brezesinski, J. Wang, S.H. Tolbert, B. Dunn, Nat. Mater. 9 (2010) 146–151.
[5] A. Walcarius, Chem. Soc. Rev. 42 (2013) 4098–4140.
[6] N. Linares, A.M. Silvestre-Albero, E. Serrano, J. Silvestre-Albero, J. García-Martínez, Chem. Soc. Rev. (2014), http://dx.doi.org/10.1039/c3cs60435g.
[7] J. Zhang, C.M. Li, Chem. Soc. Rev. 41 (2012) 7016–7031.
[8] T. Wagner, S. Haffer, C. Weinberger, D. Klaus, M. Tiemann, Chem. Soc. Rev. 42 (2013) 4036–4053.
[9] Z. Zhang, H. Song, S. Zhang, J. Zhang, W. Bao, Q. Zhao, X. Wu, CrystEngComm 16 (2014) 110–115.
[10] Z. Jin, M.D. Xiao, Z.H. Bao, P. Wang, J.F. Wang, Angew. Chem. Int. Ed. 51 (2012) 6406–6410.
[11] R. Zhang, A.A. Elzatahry, S.S. Al-Deyab, D. Zhao, Nano Today 7 (2012) 344–366.
[12] J.C. Rookea, T. Barakatb, J. Brunetb, Y. Lic, M.F. Finold, J.-F. Lamonierd, J.-M. Giraudond, R. Cousinb, S. Siffertb, B.L. Su, Appl. Catal. B: Environ. 162 (2015) 300–309.
[13] D. Carboni, D. Marongiu, P. Rassu, A. Pinna, H. Amenitsch, M.F. Casula, A. Marcelli, G. Cibin, P. Falcaro, L. Malfatti, P. Innocenzi, J. Phys. Chem. C 118 (2014) 12000–12009.
[14] L. Jing, W. Zhou, G. Tian, H. Fu, Chem. Soc. Rev. 42 (2013) 9509–9549.
[15] S.H. Shen, J. Chen, R.T. Koodali, Y.F. Hu, Q.F. Xiao, J.G. Zhou, X.X. Wang, L.J. Guo, Appl. Catal. B: Environ. 150–151 (2014) 138–146.
[16] M. Rycenga, C.M. Cobley, J. Zeng, W. Li, C.H. Moran, Q. Zhang, D. Qin, Y. Xia, Chem. Rev. 111 (2011) 3669–3712.
[17] S. Linic, P. Christopher, H. Xin, A. Marimuthu, Acc. Chem. Res. 46 (2013) 1890–1899.
[18] S.V. Boriskina, H. Ghasemi, G. Chen, Mater. Today 16 (2013) 375–386.
[19] P. Christopher, H. Xin, S. Linic, Nat. Chem. 3 (2011) 467–472.
[20] D.B. Ingram, S. Linic, J. Am. Chem. Soc. 133 (2011) 5202–5205.
[21] S. Linic, P. Christopher, D.B. Ingram, Nat. Mater. 10 (2011) 911–921.
[22] R.B. Jiang, B.X. Li, C.H. Fang, J.F. Wang, Adv. Mater. (2014), http://dx.doi.org/10.1002/adma.201400203.
[23] P. Wang, B. Huang, Y. Dai, M.-H. Whangbo, Phys. Chem. Chem. Phys. 14 (2012) 9813–9825.
[24] S.T. Kochuveedu, Y.H. Jang, D.H. Kim, Chem. Soc. Rev. 42 (2013) 8467–8493.
[25] S.A. Ansari, M.M. Khan, M.O. Ansari, J. Lee, M.H. Cho, J. Phys. Chem. C 117 (2013) 27023–27030.
[26] C. Wen, A.Y. Yin, W.L. Dai, Appl. Catal. B: Environ. 160–161 (2014) 730–741.
[27] J. Li, S.K. Cushing, J. Bright, F. Meng, T.R. Senty, P. Zheng, A.D. Bristow, N. Wu, ACS Catal. 3 (2013) 47–51.
[28] K. Awazu, M. Fujimaki, C. Rockstuhl, J. Tominaga, H. Murakami, Y. Ohki, N. Yoshida, T. Watanabe, J. Am. Chem. Soc. 130 (2008) 1676–1680.
[29] M.K. Kumar, S. Krishnamoorthy, L.K. Tan, S.Y. Chiam, S. Tripathy, H. Gao, ACS Catal. 1 (2011) 300–308.
[30] H.F. Cheng, B.B. Huang, P. Wang, Z.Y. Wang, Z.Z. Lou, J.P. Wang, X.Y. Qin, X.Y. Zhang, Y. Dai, Chem. Commun. 47 (2011) 7054–7056.
[31] H.F. Cheng, W.J. Wang, B.B. Huang, Z.Y. Wang, J. Zhan, X.Y. Qin, X.Y. Zhang, Y. Dai, J. Mater. Chem. A 1 (2013) 7131–7136.
[32] K. Fuku, R. Hayashi, S. Takakura, T. Kamegawa, K. Mori, H. Yamashita, Angew. Chem. Int. Ed. 52 (2013) 7446–7450.
[33] J. Hou, Z. Wang, C. Yang, W. Zhou, S. Jiao, H. Zhu, J. Phys. Chem. C 117 (2013) 5132–5141.
[34] A. Wolosiuk, N.G. Tognalli, E.D. Martínez, M. Granada, M.C. Fuertes, H. Troiani, S.A. Bilmes, A. Fainstein, G.J.A.A. Soler-Illia, ACS Appl. Mater. Interfaces 6 (2014) 5263–5272.
[35] W. Zhou, T. Li, J. Wang, Y. Qu, K. Pan, Y. Xie, G. Tian, L. Wang, Z. Ren, B. Jiang, H. Fu, Nano Res. 7 (2014) 731–742.
[36] Y. Wan, D. Zhao, Chem. Rev. 107 (2007) 2821–2860.
[37] L.L. Li, J. Xu, Q. Yuan, Z.X. Li, W.G. Song, C.H. Yan, Small 5 (2009) 2730–2737.
[38] Q. Lu, Z. Lu, Y. Lu, L. Lv, Y. Ning, H. Yu, Y. Hou, Y. Yin, Nano Lett. 13 (2013) 5698–5702.
[39] C. Pacholski, A. Kornowski, H. Weller, Angew. Chem. Int. Ed. 43 (2004) 4774–4777.
[40] G. Zhu, Y. Liu, H. Xu, Y. Chen, X. Shen, Z. Xu, CrystEngComm 14 (2012) 719–725.
[41] A. Tanaka, K. Hashimoto, H. Kominami, J. Am. Chem. Soc. 134 (2012) 14526–14533.
[42] S.A. Ansari, M.M. Khan, S. Kalathil, A. Nisar, J. Leea, M.H. Cho, Nanoscale 5 (2013) 9238–9246.
[43] G.Z. Xing, X.S. Fang, Z. Zhang, D.D. Wang, X. Huang, J. Guo, L. Liao, Z. Zheng, H.R. Xu, T. Yu, Z.X. Shen, C.H.A. Huan, T.C. Sum, H. Zhang, T. Wu, Nanotechnology 21 (2010) 255701.
[44] H.R. Liu, G.X. Shao, J.F. Zhao, Z.X. Zhang, Y. Zhang, J. Liang, X.G. Liu, H.S. Jia, B.S. Xu, J. Phys. Chem. C 116 (2012) 16182–16190.
[45] Z.C. Wu, C.R. Xu, Y.Q. Wu, H. Yu, Y. Tao, H. Wan, F. Gao, CrystEngComm 15 (2013) 5994–6002.
[46] Y. Zheng, L. Zheng, Y. Zhan, X. Lin, Q. Zheng, K. Wei, Inorg. Chem. 46 (2007) 6980–6986.
[47] S.S. Warule, N.S. Chaudhari, B.B. Kale, K.R. Patil, P.M. Koinkar, M.A. More, R. Murakami, J. Mater. Chem. 22 (2012) 8887–8895.
[48] P. Christopher, H. Xin, A. Marimuthu, S. Linic, Nat. Mater. 11 (2012) 1044–1050.
[49] M.C. Neves, J.M.F. Nogueira, T. Trindade, M.H. Mendonça, M.I. Pereira, O.C. Monteiro, J. Photochem. Photobiol. A: Chem. 204 (2009) 168–173.
[50] E. Grabowska, J. Reszczynska, A. Zaleska, Water Res. 46 (2012) 5453–5471.
[51] A. Mantilla, F. Tzompantzi, J.L. Fernández, J.A.I. Díaz Góngora, R. Gómez, Catal. Today 150 (2010) 353–357.
[52] C.S. Turchi, D.F. Ollis, J. Catal. 122 (1990) 178–192.
[53] J. Zhang, Y. Nosaka, J. Phys. Chem. C 118 (2014) 10824–10832.
[54] C. Avelino, A. Pedro, G. Hermenegildo, C.-C. Jean-Yves, Nat. Mater. 3 (2004) 394–397.
[55] J.-H. Hwang, T.O. Mason, Z. Phys. Chem. 207 (1998) 21–38.
[56] S.K. Cushing, J. Li, F. Meng, T.R. Senty, S. Suri, M. Zhi, M. Li, A.D. Bristow, N. Wu, J. Am. Chem. Soc. 134 (2012) 15033–15041.
[57] M. Xiao, R. Jiang, F. Wang, C. Fang, J. Wang, J.C. Yu, J. Mater. Chem. A 1 (2013) 5790–5805.
[58] Y. Zang, J. Yin, X. He, C. Yue, Z. Wu, J. Li, J. Kang, J. Mater. Chem. A 2 (2014) 7747–7753.
[59] X.J. Bai, R.L. Zong, C.X. Li, D. Liu, Y.F. Liu, Y.F. Zhu, Appl. Catal. B: Environ. 147 (2014) 82–91.